

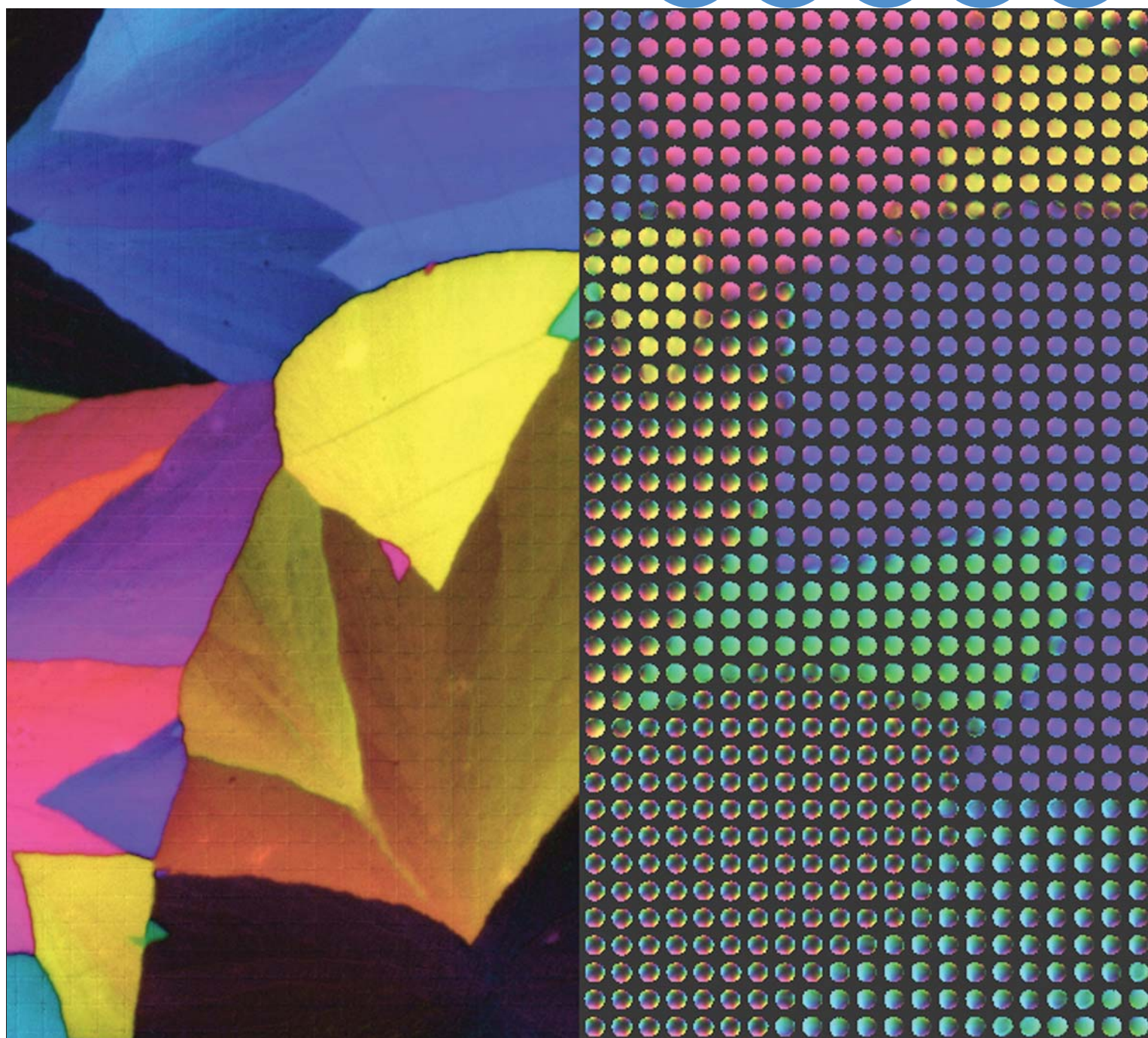
Journal of

ISSN 0022-2720

# Microscopy

Blackwell Publishing

Volume 231, Part 3, September 2008



# Polarized light field microscopy: an analytical method using a microlens array to simultaneously capture both conoscopic and orthoscopic views of birefringent objects

R. OLDENBOURG

Marine Biological Laboratory, Woods Hole, MA 02543, U.S.A.

Physics Department, Brown University, Providence, RI 02912, U.S.A.

**Key words.** Birefringence, calcite, compensator, conoscopy, electro-optical modulator, LC-PolScope, liquid crystal, optic axis, retardance, retardation.

## Summary

For the comprehensive analysis of anisotropic materials, a new approach, called ‘polarized light field microscopy’ is introduced. It uses an LC-PolScope to which a microlens array was added at the image plane of the objective lens. The system is patterned after the ‘light field microscope’ that achieves both lateral and axial resolution in thick specimens in a single camera exposure. In polarized light field microscopy, the microlens array generates a hybrid image consisting of an array of small conoscopic images, each sampling a different object area. Analysis of the conoscopic images reveals the birefringence of each object area as a function of the propagation direction of transmitted light rays. The principles and utility of the instrument that we are calling ‘light field LC-PolScope’ are demonstrated with images of a thin, polycrystalline calcite film, revealing the azimuth and inclination angle of the optic axis for many crystals simultaneously, including crystals with diameters as small as 2  $\mu\text{m}$ . Compared to traditional conoscopy and related methods, the vastly improved throughput and quantitative analysis afforded by the light field LC-PolScope make it the instrument of choice for measuring 3D birefringence parameters of complex structures.

## Introduction

The analytic power of the polarizing microscope has been greatly enhanced recently by the introduction of the LC-PolScope, which generates quantitative birefringence maps for the whole field of view at high sensitivity with both high spatial and high temporal resolution (Oldenbourg & Mei, 1995; Shribak & Oldenbourg, 2003a) (Cambridge Research and Instrumentation, Inc., Woburn,

MA; <http://www.cri-inc.com>). The LC-PolScope is one of several recent polarized light techniques that take advantage of new optical and image acquisition technologies, such as electro-optical modulators and charge-coupled device (CCD) cameras. (Otani *et al.*, 1994; Oldenbourg & Mei, 1995; Glazer *et al.*, 1996; Shribak *et al.*, 1999; Massoumian *et al.*, 2003; Kaminsky *et al.*, 2007). These advances have led to numerous new investigations in many fields, including biology where the dynamics of birefringent cytostructures are readily followed via live-cell imaging (Katoh *et al.*, 1999; LaFountain & Oldenbourg, 2004).

Polarized light microscopy is typically practiced in two, mutually exclusive observation modes, called orthoscopy and conoscopy. In orthoscopy, the specimen is viewed directly, whereas in conoscopy the ocular is replaced by a telescope lens that lets one observe conoscopic interference figures formed in the back focal plane of the objective lens (Hartshorne & Stuart, 1960). In conoscopy, the sample birefringence is measured as a function of the tilt angle of rays passing through the specimen. Hence, this observation mode reveals the inclination angle of the optic axis of a uniformly birefringent specimen region, in addition to the azimuth of the optic axis. In orthoscopy, the inclination angle, which is the angle between the optic axis and the plane of observation, is usually not evident.

However, when observing complex birefringent structures, the advantage of conoscopy in providing a more comprehensive analysis of specimen anisotropy is only gained by restricting the observation to a single uniformly birefringent specimen region. This restriction is usually achieved by closing down the field diaphragm and optically isolating a small specimen region, avoiding the confusion of superimposing conoscopic figures. Hence, the analysis of a polycrystalline calcite film, for example requires individual, conoscopic observations, one single-crystalline region at a time.

A major focus of our laboratory is the development of methods for the analysis of optical anisotropy of complex

Correspondence to: Rudolf Oldenbourg. Tel: +1-508-289-7426; fax: +1-508-540-6902; e-mail: [rudolfo@mbi.edu](mailto:rudolfo@mbi.edu)

materials. Here we present the new method of 'polarized light field microscopy' that is based on a polarizing microscope to which a microlens array is added. The microlens array is located in the image plane of the microscope's objective lens. A CCD camera behind the array captures a hybrid image that consists of a large array of small conoscopic images, each specific to a small sample area. Our technique combines an orthoscopic image of the specimen with a multitude of conoscopic images in one single camera exposure. In addition, we use the liquid-crystal universal compensator of the LC-PolScope (CRI, Woburn MA, <http://www.cri-inc.com>) to analyse the conoscopic birefringence patterns projected by each microlens for the full range of sample anisotropy, including the azimuth and inclination angle of the optic axes.

Our setup employs a design by Levoy and co-workers (Levoy *et al.*, 2006), who use a microlens array for building a so-called 'light field microscope' to reconstruct volumetric data (e.g. for resolving the lateral and axial distribution of fluorescent moieties) within a microscopic sample. In contrast, we use polarization-specific components and analyse the 3D orientations of the optic axes in a thin, polycrystalline calcite film, the model test specimen chosen for our study.

We first present an analysis of the calcite film using a regular LC-PolScope. The same calcite film is then analysed using the 'light field LC-PolScope' that includes a microlens array. We give a detailed description of the setup and illustrate its performance by recording the polarization distortions caused by the high numerical aperture (NA) objective and condenser lenses. We demonstrate the utility of the technique by analysing the 3D anisotropy of the calcite film. We compare the experimental results with model calculations, and the agreement between the two provides confidence in our approach. We then discuss alternatives for trading angular resolution for spatial resolution, as well as the exciting potential of extending the analysis of light field LC-PolScope images to reconstruct volumetric data of thick samples that have complex 3D distributions of optically anisotropic components.

## Materials and methods

### *Light field LC-Polscope*

The microlens array is made of epoxy and consists of square, plano-convex microlenses, 125  $\mu\text{m}$  on each side, with a focal length of 2.5 mm. The convex surface extends all the way to the edges of the 125  $\mu\text{m}$  square lens. The array was fabricated by Adaptive Optics Associates (now Northrop Grumman Mission Systems, Cambridge, MA) according to specifications of an array originally fabricated for Marc Levoy at Stanford University (Levoy *et al.*, 2006).

The microlens array was built into a so-called light field camera that was installed on the side port of a Zeiss Axiovert 200M (Carl Zeiss MicroImaging Inc., Thornwood, NY). In the

light field camera the back focal plane of the microlens array was imaged onto a  $2048 \times 2048$  pixel monochrome CCD camera ( $7.4 \times 7.4 \mu\text{m}^2$  pixel size, Retiga 4000R, QImaging, Surrey BC, Canada) using a 1:1 relay lens. The relay lens was assembled from two identical AF Nikkor 50 mm f/1.4D photographic lenses (Nikon, Melville NY) mounted front-to-front.

The microscope stand was equipped with LC-PolScope components, i.e. a circular polarizer and a precision universal compensator (Cambridge Research and Instrumentation, Inc.). Acquisition and initial processing of LC-PolScope images were accomplished by custom software (psj) developed in our laboratory. Additional analysis functions were implemented as plugins to ImageJ, a public domain image-processing platform (Wayne Rasband, National Institutes of Health, Bethesda MD; <http://rsb.info.nih.gov/ij/>) and as *Mathematica* Notebook functions (Wolfram Research, Inc., Champaign IL).

### *Polycrystalline calcite film*

The thin calcite film was a gift from Dr. Dirk Volkmer, University of Ulm, Germany, who has described the preparation and characterization of such films (Volkmer *et al.*, 2005). Briefly, polycrystalline calcite films are formed on a glass cover slip by starting with a metastable amorphous precursor phase that is stabilized by an anionic polymer. Subsequent heating to about 400°C for 2 h yields an optically birefringent thin film of uniform thickness of less than 1  $\mu\text{m}$ . The typical single crystal domain size is 50–150  $\mu\text{m}$ . We permanently bonded the film with cover glass to a microscope slide using an index matching resin (Permout, refractive index 1.52, Fisher Scientific, Pittsburgh, PA).

## Results

### *LC-PolScope analysis of calcite crystals*

The LC-PolScope image of a thin polycrystalline calcite film yields a birefringence map (Fig. 1) in which the hue (colour) in each image point represents the measured azimuth of the optic axis. The intensity or brightness represents the measured inclination angle of the optic axis. Within a single crystalline domain, the hue and brightness values are nearly constant, whereas abrupt changes occur across domain boundaries.

Previous studies by Volkmer and colleagues (Volkmer *et al.*, 2005) have established that the thickness of the calcite layer is constant over the field of view. Hue and brightness variations in the birefringence map shown in Fig. 1 are accounted for by the orientation of the crystallographic c-axis, i.e. the optic axis of the calcite crystals. The orientation is described by two angles, (1) the angle between the optic axis and the plane perpendicular to the microscope axis – its *inclination angle* – and (2) the angle between the projection of the optic axis



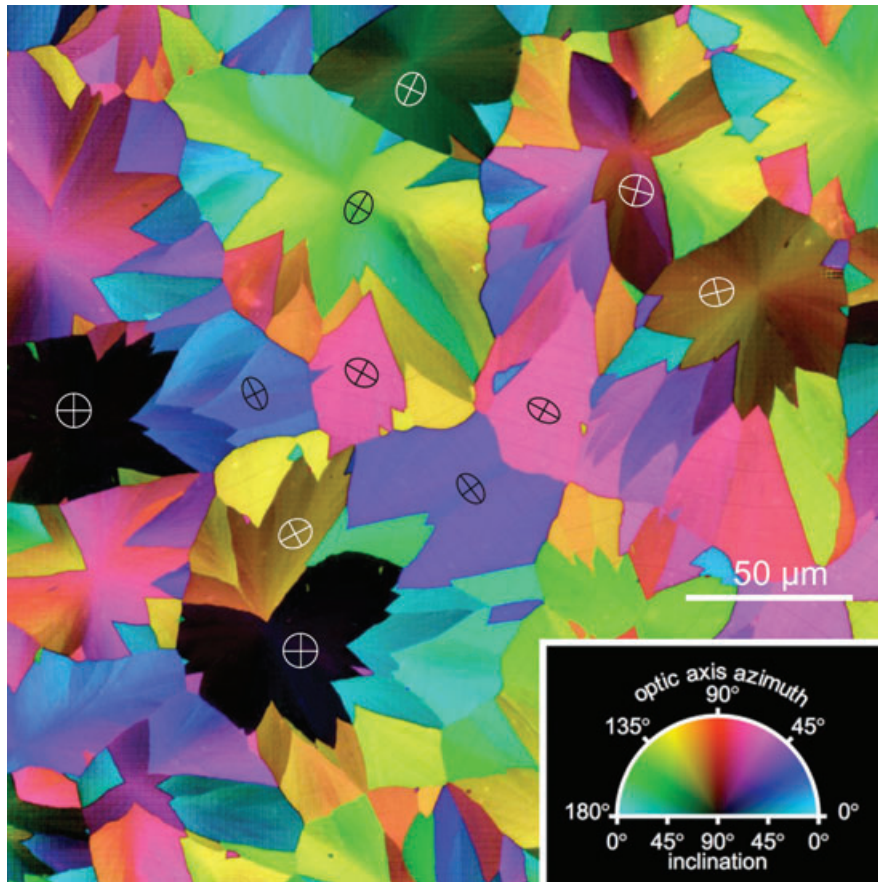


**Fig. 1.** LC-PolScope image of a thin polycrystalline calcite film of uniform thickness. In this false colour image hue represents the measured azimuth of the optic axis and brightness is proportional to the inclination angle of the optic axis (see inset). Each crystalline domain has nearly uniform hue and brightness, due to the uniform birefringence of each domain. Inside some domains we show the associated refractive index ellipse (see Fig. 2). This computed image is based on 5 raw intensity images recorded with a high resolution camera ( $2048 \times 2048$  pixels), using a  $63/1.4$  NA Plan Apochromat objective lens,  $1.4$  NA condenser lens (both oil immersion lenses), and polarization optical equipment and algorithms used in the LC-PolScope. The inset is a colour guide relating azimuth to hue, and brightness to inclination angle. Azimuth  $\phi$  (see Fig. 3) is expressed around the circumference of the semi-circle (e.g.  $0^\circ$  is pale blue;  $90^\circ$  is red). Inclination angle  $\sigma$  is expressed radially (e.g. at  $90^\circ$ , brightness is black, regardless of azimuth; at  $0^\circ$ , brightness is maximal for every azimuth).

into the same plane and the  $x$ -axis – its *azimuth angle*. In the LC-PolScope birefringence map presented in Fig. 1, the variations in azimuth lead to differently coloured crystalline domains, whereas the variations in inclination angle lead to changes in domain brightness (see insert in Fig. 1).

For an explanation of the dependence of domain brightness on inclination, refer to Fig. 2. A vertically travelling ray of polarized light passing through a domain with vertical optical axis suffers no differential phase change, hence the crystal appears isotropic and the measured retardance is zero. As the optic axis is tilted away from the vertical, more differential retardation between the principal planes of polarization occurs, and the domain appears brighter, given a thin film of constant thickness.

The work of Volkmer *et al.* (2005) showed that the inclination angle can be indirectly inferred from the measured retardance of the domain. For rays that impinge perpendicular

to the calcite film, the retardance  $\Delta$  of a crystalline domain is proportional to the square of the cosine of the inclination  $\sigma$  of the optic axis (Born & Wolf, 1980):

$$\Delta = t_{\text{film}} (n_e - n_o) \cos^2 \sigma \quad (1)$$

where  $t_{\text{film}}$  is the thickness of the calcite film, and  $n_e$  and  $n_o$  are the principal refractive indices of calcite ( $n_e - n_o = -0.174$  at  $\lambda = 546$  nm).

The hue or colour of a domain in Fig. 1 is dependent on the azimuth of the optic axis. For calcite, a negatively birefringent, uniaxial crystal, the optic axis is oriented perpendicular to the slow axis of birefringence, as illustrated in Fig. 3. The slow axis orientation for a light ray that travels parallel to the  $z$ -direction is located in the  $x$ - $y$  plane and is parallel to the long axis of the refractive index ellipse formed as the cross section between the refractive index ellipsoid of calcite and the  $x$ - $y$  plane.

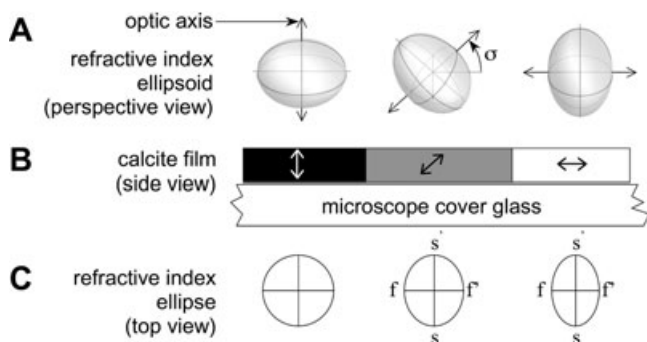


**Fig. 2.** (A) Perspective views of the refractive index ellipsoid of calcite, which is a uniaxial, negatively birefringent crystal; hence, the optic axis runs along the short axis of the ellipsoid. From left to right the oblate-shaped ellipsoids have decreasing inclination angles  $\sigma$ . (B) Schematic of thin calcite film in side view, illustrating three crystalline domains with differing orientations of their associated refractive index ellipsoids. The double-headed arrow inside each domain indicates the direction of the optic axis. The grey level of each domain represents the brightness that would be expected for such a domain in the image of Fig. 1. (C) Refractive index ellipse (cross section of index ellipsoid) for chief ray travelling perpendicular to calcite film.

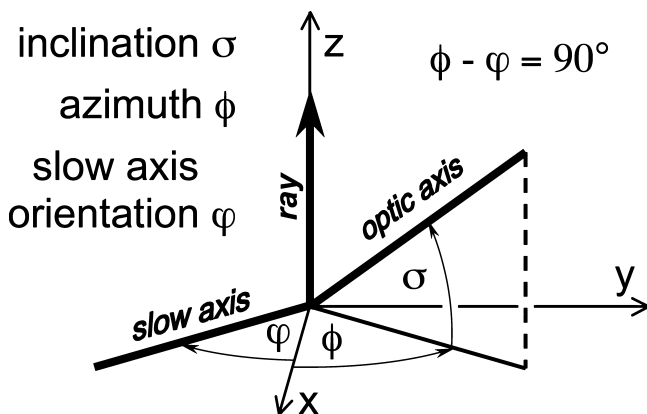


**Fig. 3.** Illustration of orientation of calcite optic axis and slow axis in object space. The slow axis is measured using light that travels chiefly along the  $z$ -direction. The calcite film extends in the  $x$ - $y$  plane, the microscope optical axis lies along the  $z$ -direction. The azimuth angle  $\phi$  of the optic axis is measured between its projection into the  $x$ - $y$  plane and the  $x$ -axis. The inclination angle  $\sigma$  is measured between the optic axis and its  $x$ - $y$  projection.

#### *LC-PolScope with microlens array: the light field LC-PolScope*

Using the same calcite film depicted in Fig. 1, we produced the grid-like birefringence map presented in Fig. 4. To obtain this image, a microlens array described in detail below was inserted into the image plane of the microscope objective lens. The CCD camera was placed behind the micro lens array, in a position where the microlenses formed images of the circular aperture or back focal plane of the objective lens. In this way, the camera captured an array of aperture images, each specific to a small region of the calcite film. Each aperture image is

formed by rays from specimen regions that are conjugate with each microlens. Thus, each aperture image maps the direction of rays from different regions of the specimen (Fig. 5).

This approach of employing a grid-like array of microlenses to 'partition' distinct regions within the specimen from one another represents a new method for measuring the 3D orientation of the optic axis directly and simultaneously for a large number of sample regions. Before giving a detailed description of how we have used this technique in the analysis of calcite crystals, we first present an outline of the design of the instrument and our image acquisition and processing procedures.

Figure 6 illustrates the optical setup, which is based on an LC-PolScope to which accessories for light field microscopy are added; thus we call it the 'light field LC-PolScope'. The optical train includes a Plan Apochromat oil immersion objective ( $63\times/1.4$  NA), an oil immersion condenser with matching NA, and a liquid crystal (LC) universal compensator. The assembly consisting of the microlens array, a relay lens, and a high-resolution CCD camera, collectively called a light field camera, is detailed as follows.

#### *Light field camera*

A photograph of the light field camera assembly is shown in Fig. 7. The optical specifications of the microlens array are chosen to match those of the imaging beam behind the objective lens. The NA of the imaging beam is 0.022, which is computed by dividing the NA on the object side of the objective ( $1.4$  NA) by the magnification of the objective ( $63\times$ ) (Inoué & Oldenbourg, 1995). The NA of the microlenses is 0.025, computed as half the microlens diameter divided by its focal length (see 'Materials and Methods'). The slightly larger NA of the microlenses compared to the NA of the imaging beam path explains the slightly smaller aperture image that is visible in Fig. 4(B), when comparing it to the pitch of the microlens array.

The relay lens, although not absolutely necessary, was included in order to make the assembly more flexible in two respects: (1) it removed the physical constraint imposed by the 2.5-mm focal length of the microlenses allowing more axial working space in the optical train and (2) it permitted easy switching between light field and conventional imaging as the microlenses are switched between two nearby positions that are separated along the optical axis by a distance equal to the focal length of the microlenses. In respect to (2) above, the switching was made possible by our design of mounting the microlens array inside a pair of concentric aluminium tubes, which could be slid relative to one another to project either the microlenses (conventional imaging) or their focal plane (light field imaging) onto the camera face plate.

In Fig. 1, the effect of a microlens array is not readily apparent, even though the array is actually present in the optical path. However, by closely examining the original image

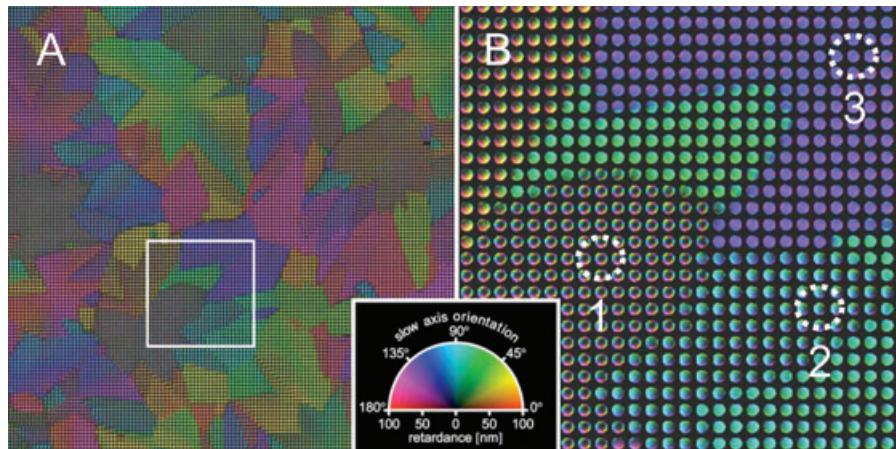


**Fig. 4.** (A): Polarized light field image of the same calcite film as shown in Fig. 1. Hue represents slow axis orientation and brightness the amount of retardance measured. The image consists of an array of  $120 \times 120$  disk-shaped images, each disk representing a circular birefringence map. A single disk maps the retardance and slow axis orientation of a small region of the film as a function of the direction of the rays that have passed through that film region. (B) A portion of the image contained in the box in (A) at higher magnification. Dotted circles target three disks whose retardance patterns are analysed in Figs 9 and 11. The image was recorded with the  $63 \times / 1.4\text{NA}$  objective lens and a micro lens array in the intermediate image plane of the objective. The inset is a colour guide showing the relationship between slow axis orientation and hue (read circumferentially), and the relationship between retardance and brightness (read radially).

of Fig. 1, one can in fact recognize the grid pattern imposed by the square edges of the microlenses. The square grid is especially visible in the corners of the image. If necessary, post-processing with an appropriately designed filter can remove this image artefact.

For acquiring Fig. 4, the microlens array was switched to a position where the back focal plane of the microlenses was projected onto the camera. We note that the required shift in the array position by 2.5 mm is smaller than the depth of focus, i.e. the distance in image space over which a given object plane remains in focus. In our case, the depth of focus is dominated by the geometric contribution  $D$  that depends on the magnification  $M$  and NA of the objective lens ( $63 \times / 1.4\text{NA}$ ) and the sampling distance  $e$  of the microlens array ( $125\text{ }\mu\text{m}$ ), as covered by Inoué and Oldenbourg (1995), ( $D = (Me)/\text{NA} = 5.6\text{ mm}$ ).

In selecting the relay lens, care must be taken that no vignetting occurs for all image points, including the outer edges of the field. Marc Levoy proposed the solution of mounting two photographic lenses front to front to achieve a relay lens with the appropriate  $f$ -number.

#### *Liquid crystal universal compensator*

The specimen is located in the polarization sensitive train spanning between the left circular polarizer and the linear analyser that is part of the LC compensator. The LC-compensator, image acquisition algorithms, and processing algorithms are the same as those available on the LC-PolScope (Cambridge Research and Instrumentation, Inc.) (Oldenbourg & Mei, 1995; Shribak & Oldenbourg, 2003a). Briefly, the LC-

compensator was operated as a variable polarization analyser. With the help of the LC-controller the LC devices were set to generate five polarization states. The first state corresponded to circular polarization, and the other states to elliptical polarizations. The elliptical polarizations had the same ellipticity, but their principal axes were sequentially rotated by  $45^\circ$ . The elliptical polarization states were generated by adding or subtracting a bias retardance of 55 nm from the circular polarization setting of the LC-devices. The acquisition of the camera images were synchronized to the polarization states, recording one image of the specimen for each polarization state (Fig. 6, panels A, B, C, D, E). Based on the five raw images, the computer generated the retardance and orientation maps.

#### *Background correction*

The performance of the setup was tested using recorded images of a sample region that was devoid of any birefringent objects. It is well known that the conoscopic image of a clear sample area reveals the spurious birefringence and differential transmission contributed by objective and condenser lenses (Inoué & Hyde, 1957). These spurious effects are typically caused by stress in lens glass and by the differential transmission and phase shift of polarized light that passes through lens surfaces and other components of the optical train (Shribak *et al.*, 2002). Figure 8 shows conoscopic images recorded with a clear sample area in view, with and without microlens array. The single conoscopic birefringence map recorded without microlens array is seen repeatedly, albeit at lower resolution, in the array of aperture images recorded with the microlenses in place.

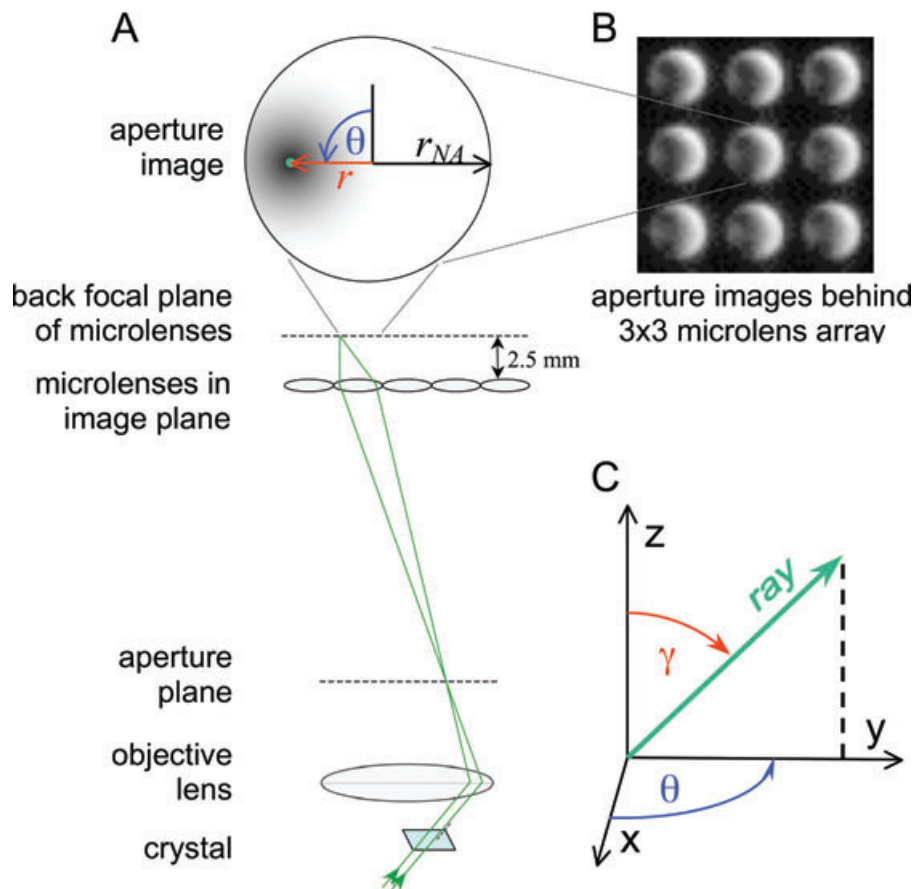


**Fig. 5.** (A) Schematic illustrating the relationship between rays that are focused into the same point of the back focal plane of the microlenses and the direction and position of those rays in object space. Near the bottom, two rays (in green) are shown travelling parallel to each other and travelling parallel to the optic axis of a small calcite crystal in object space. The rays are brought to focus in the back focal plane of the objective lens. A microlens placed in the image plane of the objective focuses the same rays into its back focal plane. Hence, each microlens projects a small image of the objective back aperture. The black spot in the aperture image is the focus of rays that travel parallel to the crystal's optic axis. The black spot position has radius  $r$  and azimuth  $\theta$ , and  $r_{NA}$  is the radius of the edge of the aperture of an objective lens with numerical aperture NA. The light intensity behind a microlens is dark beyond radius  $r_{NA}$ , as is evident in (B), the image behind a  $3 \times 3$  microlens array. (C) A perspective drawing of the ray direction in object space that is associated with the centre of the dark spot in the aperture image. The tilt angle  $\gamma$  is related to the radius  $r$  in the aperture plane (see text). The azimuth  $\theta$  is the same in the aperture plane as in object space.

The light field image shown in Fig. 8(B) constitutes what we call a background birefringence map. This background map is due to the polarization aberrations caused by the objective lens, condenser lens and other components in the polarization optical train and superimposes on every measurement that is recorded with the light field LC-PolScope. To remove the effect of this spurious birefringence from sample images we applied a background correction procedure that was developed for the LC-PolScope (Shribak & Oldenbourg, 2003a). The procedure requires the recording of a background birefringence map as shown in Fig. 8(B) and the subtraction of the effect of the background map from a sample map. All birefringence maps of calcite films shown in Figs 1, 4, 6, 9 and 11 were corrected using an appropriate background map.

#### *Light field LC-PolScope analysis of calcite crystals*

In further characterizing the performance of the light field LC-PolScope, we have analysed the birefringence patterns recorded in images of the thin calcite film shown in Fig. 4.

With the addition of the microlenses, the retardance and orientation maps reveal the inclination of the optic axis in each sample region. Fig. 9 shows a retardance and orientation map recorded behind a single microlens. In the  $13 \times 13$  pixel map one recognizes a dark spot surrounded by a nearly circular pattern of retardance. Rays that are focused in the centre of the dark spot have travelled parallel to the optic axis in the small crystalline sample region that was projected onto the microlens. Because rays in the centre of the dark spot have travelled parallel to the optic axis, their polarization remained



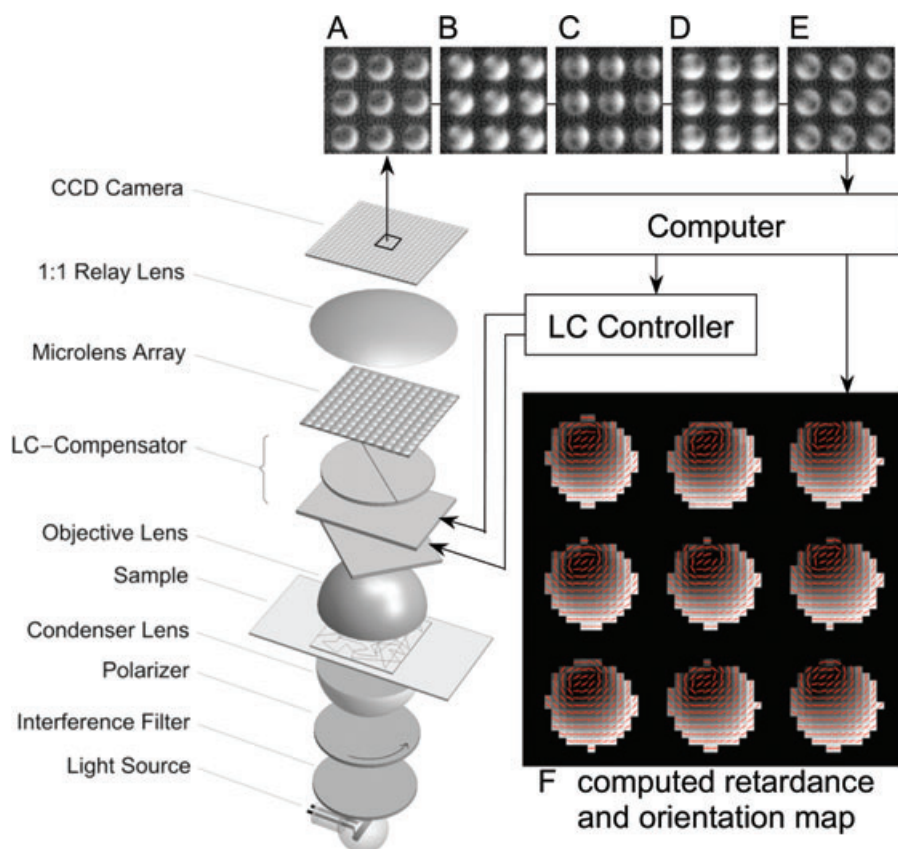


**Fig. 6.** Schematic of Light Field LC-PolScope including the optical setup with image acquisition and processing components. The optical parts include the light source (100W halogen lamp), interference band pass filter (wavelength 546 nm/10 nm band pass), left circular polarizer, condenser lens (oil, NA 1.4), sample (calcite film), objective lens (Plan Apo 63 $\times$ /1.4 NA oil), universal compensator made of two liquid crystal (LC) variable retarder plates and a linear polarizer (Cambridge Research and Instrumentation Inc.), microlens array (placed in objective image plane), and a 1:1 relay lens, which images the back focal plane of the microlenses onto the camera. (A–E) Complete analysis of the polarized light field requires 5 images; each image shown is a 52 $\times$ 52 sub-region of the five 2048 $\times$ 2048 pixel images actually acquired, each image recorded at one of the five settings of the LC-compensator. (F) Based on the raw intensity images, the computer calculates a retardance and an orientation map, shown here as a composite image with red lines indicating the slow axis orientation. The computer synchronizes the raw image acquisition with the compensator settings using a serial connection to the LC controller.

unchanged, and the measured retardance is zero. The paths of rays that were focused elsewhere in the circular pattern were tilted with respect to the optic axis and hence, the measured retardance is non-zero.

As demonstrated below, the observed retardance map behind each micro lens can be analysed in terms of the orientation of the optic axis and the direction of the rays passing through the crystals. Figure 10 illustrates the geometric relationship between the optic axis orientation and the direction of a ray passing through the calcite film. A polarized light ray propagating through the crystal in a given direction accumulates a differential phase shift that is expressed as retardance. The total retardance depends both (1) on the angle  $\beta$  between the optic axis and the ray direction and (2) on the physical path length of the ray through the crystal. Equation (1) can be generalized to account for these

dependencies (Born & Wolf, 1980):

$$\Delta = \frac{t_{\text{film}}}{\cos \gamma} (n_e - n_o) \sin^2 \beta, \quad (2)$$

with  $t_{\text{film}}$  the film thickness and  $\gamma$  the tilt angle of the ray;  $t_{\text{film}}/\cos \gamma$  is the physical path length. The angle  $\beta$  is a function of the tilt  $\gamma$  and azimuth  $\theta$  of the ray and the inclination  $\sigma$  and azimuth  $\phi$  of the optic axis:

$$\begin{aligned} \cos \beta = & \cos \theta \cos \sigma \cos \phi \sin \gamma + \cos \gamma \sin \sigma \\ & + \cos \sigma \sin \gamma \sin \theta \sin \phi \end{aligned} \quad (3)$$

The azimuth and tilt angle of a ray in object space are related to the radius and azimuth of the point through which the ray passes in the aperture of the objective lens (see Fig. 5). For an objective lens that fulfils Abbe's sine condition, one can show that rays that pass through a point with radius  $r$  in the



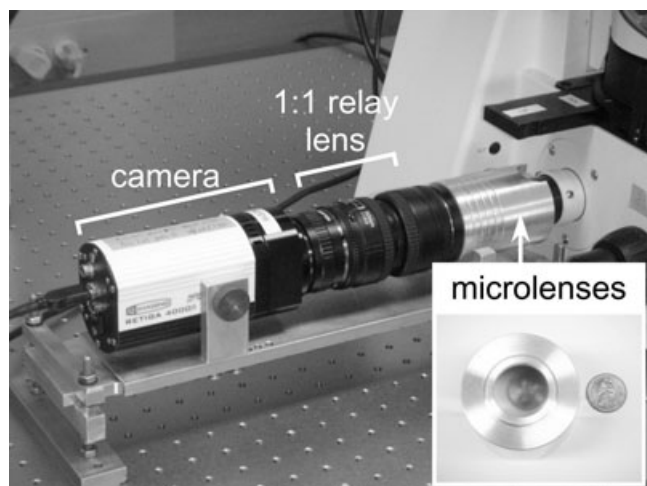


**Fig. 7.** Light field camera mounted to the side port of the microscope stand. The inset shows the microlens array in its aluminium tube after it was removed from the assembly and stood upright on a white surface. A penny was laid behind the lens array to demonstrate the blurring effect of the microlenses.

aperture plane have a tilt angle  $\gamma$  that is related to  $r$  by:

$$\sin \gamma = \frac{r}{r_{\text{NA}}} \frac{\text{NA}}{n_{\text{Medium}}}, \quad (4)$$

where  $n_{\text{Medium}}$  is the refractive index of the medium imbibing the object and  $r_{\text{NA}}$  is the radius of the full aperture of an objective lens with a numerical aperture NA. As illustrated

in Fig. 5, the azimuth  $\theta$  of the point in the aperture is equal to the azimuth  $\theta$  of the ray in object space.

In addition to the retardance, the map in Fig. 9 also shows an array of short red lines, one in each pixel location. Each line indicates the measured orientation of the slow axis. As for the retardance, the slow axis that is measured in a given point of the aperture is associated with the rays' propagation direction through the calcite film. Points in the aperture plane that are located on a circle around the optic axis point correspond to rays that pass through the film in directions that lie on the surface of a cone, with the optic axis at the centre of the cone. In addition, the measured slow axis orientation in an aperture point derives from the projection of the refractive index ellipsoid of the calcite film onto the plane perpendicular to the ray direction in the film. This leads to the near circular symmetry of the pattern of retardance and slow axis lines in Fig. 9, with the optic axis point at the centre of the circular pattern. Because calcite is negatively birefringent, the lines are tangentially rather than radially arranged.

The geometry of the retardance patterns, like the one in Fig. 9, exhibits only approximate circular symmetry with respect to the optic axis point, because of the thin slab geometry of the calcite film. By way of explanation, rays that pass close to the outer edge of the aperture have large tilt angles in object space. As illustrated in Fig. 10, rays with a large tilt angle have a long physical path length through the film. With increasing path length, the measured retardance also increases, causing increasingly greater retardance values as the rays pass closer to the aperture edge.

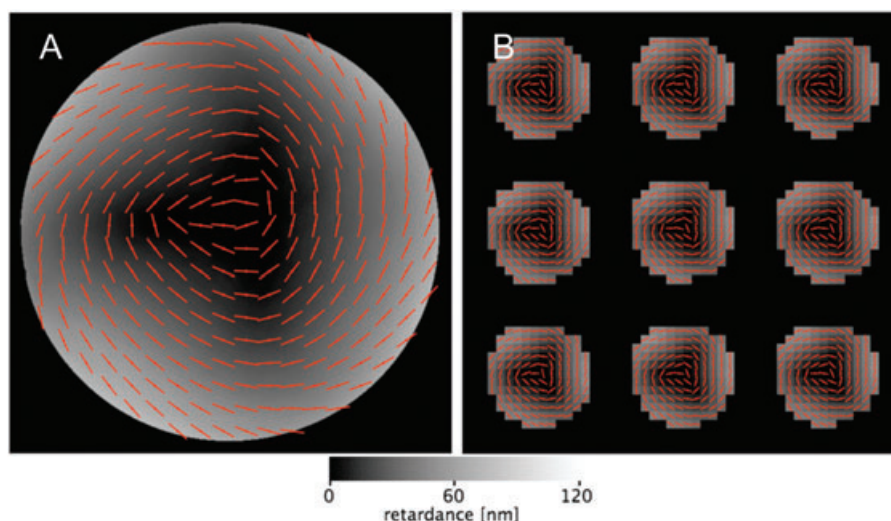


**Fig. 8.** (A) Birefringence map of the objective aperture recorded with the LC-PolScope while imaging a sample area devoid of birefringence. Retardance values increase from the centre towards the edge of the aperture resulting from polarization aberrations primarily caused by high numerical aperture (NA) lenses ( $63\times/1.4$  NA Plan Apochromat oil immersion objective, and  $1.4$  NA oil immersion condenser lens). The red lines indicate slow axis orientations. For imaging the objective aperture a Bertrand lens was added to the imaging path behind the universal compensator. (B) Birefringence map of a clear sample area, using the same objective and condenser lenses, but recorded with the light field LC-PolScope (without Bertrand lens). The small clip illustrates the near exact repeat of the conoscopic birefringence map shown in panel A behind each of the  $3\times 3$  microlenses, albeit at lower resolution. Panel B also illustrates a portion of the background map that was used to remove spurious birefringence from sample images (see text).

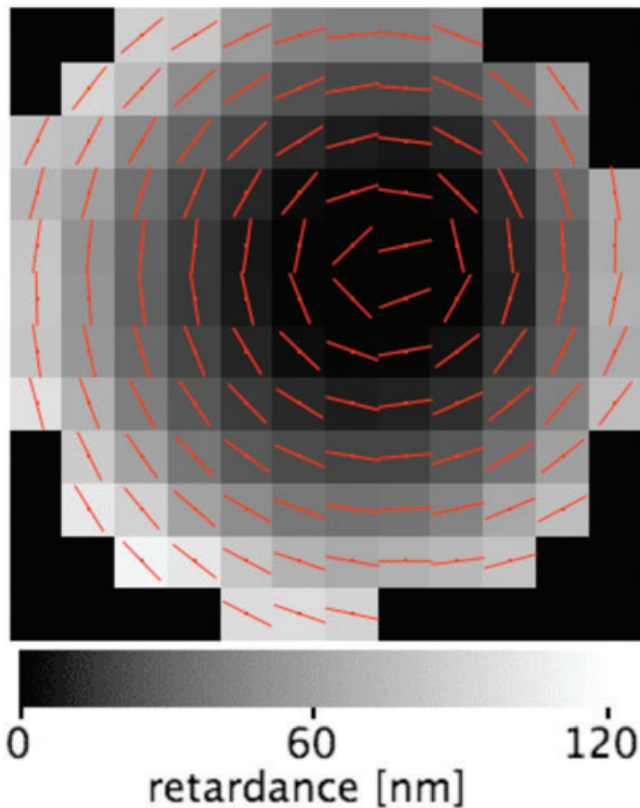


Fig. 9. Retardance and orientation map of a calcite crystal imaged by a single microlens (circled area 1 in Fig. 4(B)). The circular pattern behind the microlens is mapped onto a square of  $13 \times 13$  pixels. For each pixel, a retardance value and slow axis orientation (red line) are indicated. The dark centre shifted towards the 2 o'clock position in the pattern corresponds to the optic axis orientation (see Fig. 5). Note that the slow axes (red lines) are oriented nearly perpendicular to the line connecting a given pixel with the centre of the dark spot. The black corners of the square correspond to image regions that are located outside the aperture image and receive little or no light. Underexposed pixels are not evaluated and their retardance is set to zero.

Figure 11 shows several aperture patterns recorded for different crystalline regions of the calcite film. Each pattern is associated with a graph of retardance values that were measured along a line through the centre of the aperture and through its optic axis point (blue points). The graphs include predicted values that we calculated using Eqs (2)–(4). The adjustable parameters in this set of equations are the film thickness, and the inclination and azimuth angle of the optic axis. In the specimen used, the thickness is expected to be the same throughout the film, whereas the optic axis orientation changes from one crystalline region to another.

Figure 11(D) summarizes our results of analysing the aperture patterns of six different calcite crystals. The plot shows the apparent birefringence  $\Delta n$  as a function of the direction of the rays as they traverse the crystal. The direction is given as the angle  $\beta$  between the ray and the crystal's optic axis.

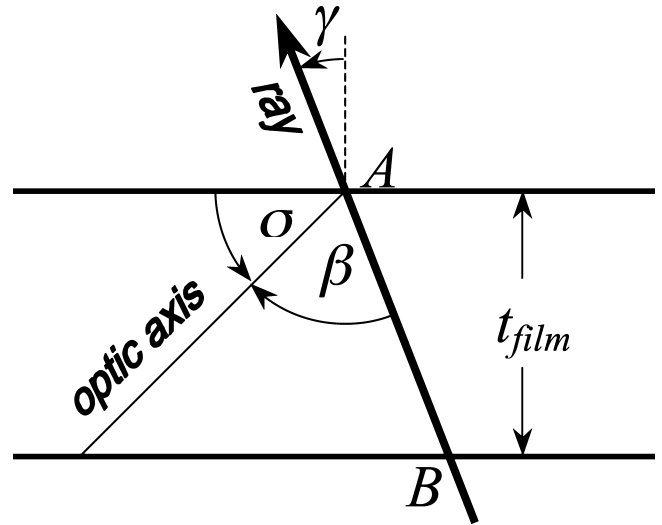


Fig. 10. The geometric relationship of the optic axis and a ray path traversing the thin calcite slab. Because the calcite film is abutted by index matching materials (glass and embedding resin), refractive bending of the ray at the crystal surfaces is minor and is not shown in the illustration. The physical path length of the ray is the distance  $AB$ .

The apparent birefringence  $\Delta n$  is expressed as the retardance  $\Delta$  measured in a given aperture point divided by the physical path length through the crystal of rays that are focused in that aperture point. The theoretical expectation for  $\Delta n$  is based on Eq. (2):

$$\Delta n = \frac{\Delta}{t_{\text{film}} / \cos \gamma} = (n_e - n_o) \sin^2 \beta,$$

with  $(n_e - n_o) = -0.174$  for calcite and the assumption of a uniform crystal thickness  $t_{\text{film}} = 310$  nm. The angle  $\beta$  is calculated as the angle between the ray in the medium and the crystal's optic axis. This seems justified as the film is embedded in a resin whose refractive index (1.52) quite closely matches the average refractive index of calcite (1.59). Therefore, the effect of refraction at the crystal's surface is minor compared to the experimental uncertainties in our measurements.

In each of the experimental patterns in Fig. 11, the predicted values match remarkably well the measured values, assuming the uniform film thickness of 310 nm. The optic axis orientation has the most profound impact on the retardance pattern observed behind each microlens. In cases where the inclination  $\sigma$  is sufficiently large, the pattern has a clear minimum, which can be used to determine  $\sigma$  and the azimuth  $\phi$  of the optic axis. The azimuth  $\phi$  can also be inferred from the slow axis orientation  $\varphi_{\text{centre}}$  measured in the centre of the aperture ( $\phi = \varphi_{\text{centre}} + 90^\circ$ ). In generating the best fits shown in Fig. 10, we considered all these dependencies and minimized the deviations between the measured and calculated values by manually exploring an appropriate parameter space for film thickness, and inclination and azimuth angles of the optic axis.

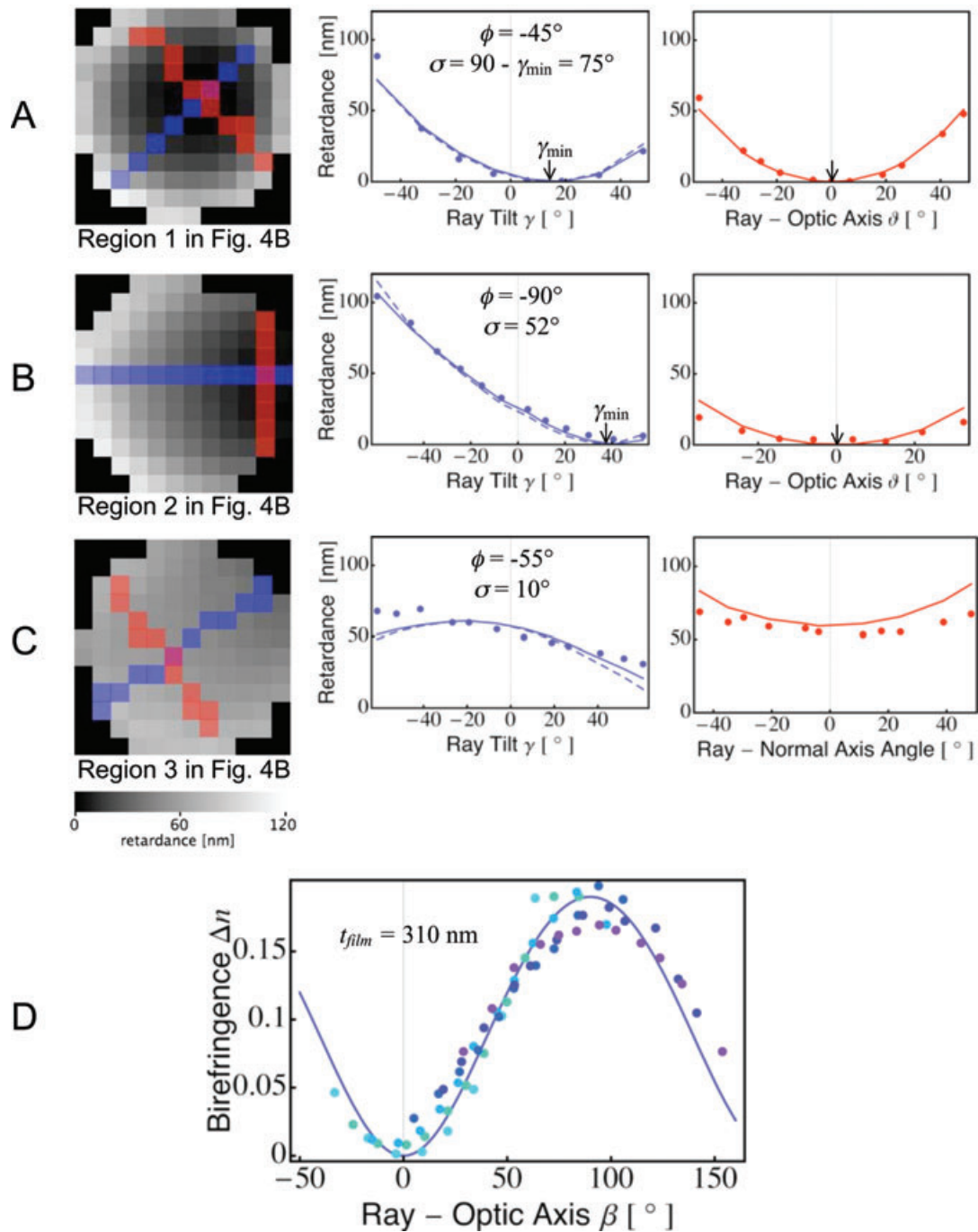


**Fig. 11.** Analysis of retardance patterns recorded behind single micro lenses outlined in Fig 4: (A) region 1 circled in Fig 4(B), (B) region 2 in 4B, (C) region 3 in 4B. The patterns shown on the left were used to generate the line plots to the right. The blue and red tinted pixels were used to draw correspondingly coloured plot values. For (A) and (B), the blue tinted pixels form a line passing through the aperture centre and the optic axis location. The red tinted pixels form a line through the optic axis location and extend perpendicular to the blue pixel line. The small, down-pointing arrows in the plots indicate the optic axis location in each plot. For (C), the optic axis location is beyond the recorded aperture. Therefore, in this case we chose the crossover of the red and blue pixel lines to be the normal to the optic axis. Best fits of theoretical expectations to measured values were obtained assuming a uniform film thickness of 310 nm and values of optic axis inclination  $\sigma$  and azimuth  $\phi$  as indicated in the graphs. Solid lines plot results using an exact theory, whereas the dashed lines were calculated using the approximation that the birefringence of calcite is small compared to its absolute refractive index values. (D) The apparent birefringence  $\Delta n$ , measured as retardance divided by physical path length, is plotted versus the angle  $\beta$  between the ray direction and optic axis orientation. Solid circle values are based on blue line measurements taken from six different crystalline regions. The continuous line represents the theoretical expectation (see text).



The remaining systematic deviations between the experimental and theoretical values have several origins. One possible reason is the approximation on which the derivation of Eqs (1) and (2) is based. To check the validity of the assumption that  $(n_e - n_o) = -0.174$  can be treated as small compared to the absolute values of  $n_e = 1.488$  and  $n_o = 1.662$ , we analysed the patterns using the exact expressions published by Born and Wolf (1980). In the Appendix, we outline our solution of the complete set of expressions for the expected retardance versus the ray direction through the crystal. In the graphs of Fig. 11, the approximate and the exact results are shown as dashed and solid lines, respectively. It is evident that there is negligible difference between the two approaches, and therefore the approximation seems well justified for thin calcite films.

Another reason for the systematic deviations between expected and measured retardance values is the spurious birefringence of the objective and condenser lenses. The algorithms for removing those contributions work best if the background retardance is small (Shribak & Oldenbourg, 2003a). As seen in Fig. 8, the background retardance varies across the aperture, generally being low near the centre and reaching a maximum of up to 50 nm near the edge of the aperture. Improved correction algorithms, such as those described in (Oldenbourg, 2002), are likely to reduce the effect of the spurious birefringence contributed by optical elements other than the sample itself.

## Discussion

Existing methods for analysing the 3D optical anisotropy of composite materials have very limited capability to analyse large, heterogeneous fields. In addition to traditional conoscopy, which we presented in the 'Introduction', one can use a polarizing microscope equipped with a rotation stage that allows rotation of the specimen around two or more orthogonal axes. In the so-called universal stage invented by Fedorov more than 100 years ago (Hartshorne & Stuart, 1964) the specimen is mounted between two glass hemispheres. The spindle stage by Bloss (1981) can be used for small crystals immersed in an index matching liquid. More recently, Glazer and collaborators have built motorized goniometric stages for this purpose (Kaminsky & Glazer, 1996; Pajdzik & Glazer, 2006). Rotation of the specimen through measured angles around two or more axes allows one to explore the birefringence patterns of a small specimen region that is located in the common centre of rotation. Therefore, like in conoscopy, rotation stages limit the measurement of complex anisotropic materials to small regions, one region at a time.

Recently, Shribak & Oldenbourg (2003b, 2004) have introduced an alternative technique for measuring the inclination and azimuth of the optic axis of uniaxial birefringent samples at high spatial resolution. This technique also builds on the LC-PolScope and adds a rotatable asymmetric mask to the front aperture of a high NA condenser.

By rotating the opening of the mask to different locations in the aperture, the chief ray of the illuminating beam is tilted to different angles, implementing a microscopy technique that uses variable oblique illumination. Images of the specimen are recorded for a small number of tilt angles and are combined to reveal the anisotropy and optic axis orientation in its azimuth and inclination angle for every resolved specimen point. The technique, called the scanned aperture LC-PolScope, largely preserves the lateral resolution as defined by the NA of the objective lens.

Such alternatives require significant modifications to the microscope setup to allow for the 3D analysis of birefringence parameters. For a similar analysis, the polarized light field approach introduced here only requires the replacement of the regular camera with a light field camera of the design proposed by Ren Ng and Marc Levoy (Ng *et al.*, 2005; Levoy *et al.*, 2006). However, as discussed in the following section, in such a camera the spatial resolution is usually reduced and is linked to the angular resolution of the light field camera.

### *The tradeoff between spatial versus angular resolution*

With the addition of the microlens array, angular resolution is gained at the expense of spatial resolution. In our current setup, for example the spatial resolution is reduced to 2  $\mu\text{m}$ , compared to the 0.2  $\mu\text{m}$  that can be achieved when using the same objective lens without the microlens array. The spatial resolution of the light field microscope is directly related to the pitch of the microlens array and the magnification of the objective lens. In our case, we used a microlens array with 125  $\mu\text{m}$  pitch and a  $63\times/1.4$  NA objective lens. The 63 times magnified image of the calcite film is sampled by a microlens every 125  $\mu\text{m}$ . Hence, the sampling rate in object space is  $125/63$  or almost 2  $\mu\text{m}$ .

Angular resolution in the light field microscope depends on the diameter of the image of the objective aperture projected behind each microlens and on the size of the camera pixels. Using geometric optics, we estimate the diameter of the objective aperture image to be about 110  $\mu\text{m}$  in our setup. The circular pattern is sampled by square camera pixels, each  $7.4 \times 7.4 \mu\text{m}^2$ . The pixel positions and spacing can be related to the tilt angle  $\gamma$  using Eq. (4). Because the expression involves the sine of  $\gamma$ , the angular resolution is best in the centre of the pattern and gets progressively worse towards the edge. Near the centre the angular step size is about  $4^\circ$ , whereas near the edge the step size between adjacent pixels is  $8^\circ$  (see graphs in Fig. 11(A–C)).

Spatial resolution can be increased at the expense of the angular resolution of the light field camera. For example, assuming we keep the microscope objective the same, one can reduce the pitch of the microlens array to increase spatial resolution. In so doing one has to also reduce the focal length of the micro lenses to keep the microlens NA (the ratio of half the pitch to focal length) equal to the image NA of the microscope

objective. Reducing the focal length of the microlenses reduces the size of the aperture image on the camera, and in turn increases the angular step size between adjacent camera pixels, which is tantamount to reducing angular resolution.

Angular resolution is also affected by diffraction. In the focal plane behind each micro lens a diffraction pattern is formed of the square aperture of the lens. The central diffraction feature has a full width at half maximum of  $d = 2 \lambda f/a$ , with wavelength  $\lambda$ , focal length  $f$  and microlens width  $a$  [see e.g. (Hecht, 2002)]. After inserting the appropriate values for our case, we find the diameter of the central diffraction feature to be about  $d = 22 \mu\text{m}$ . This means that every feature of the objective aperture image is broadened by diffraction to a minimum diameter of  $22 \mu\text{m}$ . Hence, the camera's pixel width of  $7.4 \mu\text{m}$  provides adequate sampling of the diffraction limited aperture image. Interestingly, reducing the array pitch with concomitant reduction of the focal length of the microlenses leaves the size of the diffraction pattern unchanged (see above expression for  $d$ ). Hence, the same camera still samples the aperture image correctly, even if the pitch and focal length of the microlenses are reduced for better spatial resolution.

An additional point is that the sensitivity of the light field LC-PolScope is improved by recording high-resolution conoscopic images. For an explanation consider Fig. 8(A), a conoscopic image of the objective back aperture. The polarization aberrations caused by either strain in glass and/or differential transmission and refraction on optical elements are clearly distinct in this conoscopic image (Fig. 8(A)) and in the corresponding light field images (Fig. 8(B)). Therefore, the background correction procedure can explicitly account for these aberrations and partially remove their effect from the sample measurements. However, if angular resolution is decreased, then the accuracy of the recorded background retardance is also decreased, resulting in a less accurate background correction. For best results, polarization aberrations should be removed optically by devices proposed by Inoué and colleagues (Inoué & Hyde, 1957; Shribak *et al.*, 2002).

#### *Applications to the analysis of thick birefringent specimens*

We are most excited by the potential of extending this approach to analyse thick birefringent specimens. The instrument itself need not be modified to acquire useful images of materials that are more complex and thicker than the calcite film used here.

The foundation on which our setup was designed is the light field microscope developed by Levoy and co-workers and aimed precisely at the simultaneous recording of 3D image data. Thus, with the extension of this approach to polarized light microscopy, we think the new technique of 'polarized light field microscopy' will have many diverse applications in the future.

For the analysis of polarized light field images of thick specimens, the variation of the optic axis orientation across a single object plane, as recorded in a polarized light field image, is confounded by the superposition of image data from nearby object planes. In analysing this superposition and disentangling it, it might be possible to use a tomographic approach, similar to the one published by Aben *et al.* (2005) and by Schupp (1999). Although it seems a formidable task to develop algorithms that can accomplish such an analysis across birefringence maps recorded with the light field LC-PolScope, we believe it is well worth the effort to expand the unique analytical power of the polarizing microscope in this way.

In preparing the light field LC-PolScope for routine operations, either for the analysis of thick or thin birefringent samples, efficient software tools will have to be developed. Most any array size, including the  $120 \times 120$  microlenses used for the current study, is too large to be fully analysed in the way demonstrated in Fig. 11. For a comprehensive analysis, an automated procedure must be developed that determines the anisotropy, including the inclination and azimuth of the optic axis, for each resolved sample area based on the available aperture image. Such an automated procedure can use either numerical fitting and/or analytic solutions. Furthermore, new visualization techniques are required to give an intelligible, comprehensive view of the multiple values measured in each resolved sample area.

In conclusion, the relatively simple modification of replacing the traditional camera on a polarizing microscope with a light field camera offers a new way for the comprehensive study of complex materials. The significance and impact of this new technology is only limited by the depth of our understanding of the physical optics governing the image forming process, by the efficiency of the software tools to be developed, and by our imagination in finding exciting applications in biology, chemistry, physics, and other areas of science, medicine and industry.

#### **Acknowledgements**

I am grateful for important contributions made by the following individuals: Marc Levoy of Stanford University, for extensive discussions and scientific exchange on the design of the light field camera and the optical properties of light fields; Dirk Volkmer of the University of Ulm, Germany, for generously providing the thin calcite film; Shinya Inoué and Michael Shribak of the MBL, for stimulating discussions on the design of the instrument and its potential applications; James R. LaFountain, Jr., of the University at Buffalo, for improving the clarity of the manuscript; Grant B. Harris of the MBL, for software design and technical support, Robert Knudson of Technical Video, Ltd., for fabricating microscope parts as needed, and Rudi Rottenfusser of Carl Zeiss, Inc., for advise and support of microscope instrumentation. The

work was supported by a grant from the National Institute of Biomedical Imaging and Bioengineering, EB002583, and through financial assistance from the Japan Science and Technology Corporation through a grant awarded to Yoshinori Fujiyoshi of Kyoto University, Japan.

## References

- Aben, H., Errapart, A., Ainola, L. & Anton, J. (2005) Photoelastic tomography for residual stress measurement in glass. *Opt. Eng.* **44**, Art. No. 093601.
- Bloss, F.D. (1981) *The Spindle Stage. Principles and Practice*. Cambridge University Press, Cambridge.
- Born, M. & Wolf, E. (1980) *Principles of Optics*. Pergamon Press, Elmsford, NY.
- Glazer, A.M., Lewis, J.G. & Kaminsky, W. (1996) An automatic optical imaging system for birefringent media. *Proc. R. Soc. London, A* **452**, 2751–2765.
- Hartshorne, N.H. & Stuart, A. (1960) *Crystals and the Polarising Microscope: a Handbook for Chemists and Others*. Arnold, London.
- Hartshorne, N.H. & Stuart, A. (1964) *Practical Optical Crystallography*. American Elsevier Publishing Co., Inc., New York, NY.
- Hecht, E. (2002) *Optics*. Pearson/Addison-Wesley, San Francisco, CA.
- Inoué, S. & Hyde, W.L. (1957) Studies on depolarization of light at microscope lens surfaces II. The simultaneous realization of high resolution and high sensitivity with the polarizing microscope. *J. Biophys. Biochem. Cytol.* **3**, 831–838.
- Inoué, S. & Oldenbourg, R. (1995) Microscopes. *Handbook of Optics* (ed. by M. Bass), 2nd edn. McGraw-Hill, Inc., New York.
- Kaminsky, W. & Glazer, A.M. (1996) Measurement of optical rotation in crystals. *Ferroelectrics* **183**, 133–141.
- Kaminsky, W., Gunn, E., Sours, R. & Kahr, B. (2007) Simultaneous false-colour imaging of birefringence, extinction and transmittance at camera speed. *J. Microsc.* **228**, 153–164.
- Kato, K., Hammar, K., Smith, P.J. & Oldenbourg, R. (1999) Birefringence imaging directly reveals architectural dynamics of filamentous actin in living growth cones. *Mol. Biol. Cell.* **10**, 197–210.
- LaFountain, J.R., Jr. & Oldenbourg, R. (2004) Maloriented bivalents have metaphase positions at the spindle equator with more kinetochore microtubules to one pole than to the other. *Mol. Biol. Cell.* **15**, 5346–5355.
- Levoy, M., Ng, R., Adams, A., Footer, M. & Horowitz, M. (2006) Light Field Microscopy. *ACM Transactions on Graphics*, **25**, 924–934.
- Massoumian, F., Juskaitis, R., Neil, M.A. & Wilson, T. (2003) Quantitative polarized light microscopy. *J. Microsc.* **209**, 13–22.
- Ng, R., Levoy, M., Bredif, M., Duval, G., Horowitz, M. & Hanrahan, P. (2005) Light field photography with a hand-held plenoptic camera. *Stanford Tech. Report. CTSR*, 2005–02.
- Oldenbourg, R. (2002) Retardance measurement method. In: *US Patent, Number 6,501,548*. Cambridge Research & Instrumentation Inc., Woburn, MA.
- Oldenbourg, R. & Mei, G. (1995) New polarized light microscope with precision universal compensator. *J. Microsc.* **180**(2), 140–147.
- Otani, Y., Shimada, T., Yoshizawa, T. & Umeda, N. (1994) Two-dimensional birefringence measurement using the phase shifting technique. *Opt. Eng.* **33**, 1604–1609.
- Pajdzik, L.A. & Glazer, A.M. (2006) Three-dimensional birefringence imaging with a microscope tilting-stage. I. Uniaxial crystals. *J. Appl. Crystallogr.* **39**, 326–337.
- Schupp, D. (1999) Optische Tensortomographie zur Bestimmung räumlicher Spannungsverteilungen. *Technisches Messen* **66**, 54–60.
- Shribak, M., Inoué, S. & Oldenbourg, R. (2002) Polarization aberrations caused by differential transmission and phase shift in high NA lenses: theory, measurement and rectification. *Opt. Eng.* **41**, 943–954.
- Shribak, M. & Oldenbourg, R. (2003a) Techniques for fast and sensitive measurements of two-dimensional birefringence distributions. *Appl. Opt.* **42**, 3009–3017.
- Shribak, M. & Oldenbourg, R. (2003b) Three-dimensional birefringence distribution in reconstituted asters of *Spisula* oocytes revealed by scanned aperture polarized light microscopy. *Biol. Bull.* **205**, 194–195.
- Shribak, M. & Oldenbourg, R. (2004) Mapping polymer birefringence in three dimensions using a polarizing microscope with oblique illumination. *SPIE Proceedings (Proc. Biophotonics Micro- and Nano-Imaging)*, **5462**, 57–67.
- Shribak, M.I., Otani, Y. & Yoshizawa, T. (1999) Return-path polarimeter for two dimensional birefringence distribution measurement. *SPIE Proceedings (Proc. Polarization: Measurement, Analysis, and Remote Sensing II)*, **3754**, 144–149.
- Volkmer, D., Harms, M., Gower, L. & Ziegler, A. (2005) Morphosynthesis of nacre-type laminated CaCO<sub>3</sub> thin films and coatings. *Angew. Chem. Int. Ed. Engl.* **44**, 639–644.

## Appendix

We calculated the expected retardance of a calcite film based on a set of expressions published by Born & Wolf (1980). Equations (1) and (2) in the current article are based on the approximation that the birefringence ( $n_e - n_o$ ) = −0.174 is small compared to the absolute values of  $n_e = 1.488$  and  $n_o = 1.662$ . Because the birefringence is larger than 10% of the absolute values we also solved the exact expressions as detailed below.

A light ray passing through a uniaxial birefringent crystal is typically split into two components, which have orthogonal polarization and travel in two slightly different directions through the crystal. One ray component is polarized perpendicular to the optic axis and is refracted according to the laws of refraction with the refractive index  $n_o$ . Hence, an ordinary ray that has a tilt angle  $\gamma$  in the medium surrounding the calcite film will have a tilt angle  $\gamma'$  inside the calcite film that satisfies the law of refraction:

$$n_o \sin(\gamma') = n_{\text{medium}} \sin(\gamma)$$

The extraordinary ray is refracted into a slightly different direction compared to the ordinary ray and we call its tilt angle  $\gamma''$ . The extraordinary ray is retarded according to the refractive index  $n''$  that is a function of the propagation direction of this ray with respect to the optic axis:

$$n''(\beta'') = \sqrt{\frac{\cos^2(\beta'')}{n_o^2} + \frac{\sin^2(\beta'')}{n_e^2}} \quad (5)$$



where  $\beta''$  is the angle between the direction of the extraordinary ray and the optic axis. The refraction of the extraordinary ray also fulfils the law of refraction:

$$n''(\beta'') \sin(\gamma'') = n_{\text{medium}} \sin(\gamma). \quad (6)$$

The parameters  $\beta''$  and  $\gamma''$  are geometrically related to each other by the expression for the angle between the extraordinary ray and the optic axis:

$$\cos(\beta'') = \cos(\gamma'') \sin(\sigma) + \sin(\gamma'') \cos(\sigma) \cos(\theta - \phi), \quad (7)$$

with  $\sigma$  the inclination and  $\phi$  the azimuth of the optic axis, and  $\theta$  the azimuth of the extraordinary ray (note that the ray azimuths inside and outside the calcite film are the same). For

a ray that is imaged into an aperture position  $(\theta, r)$  (see Fig. 5), the parameters  $\gamma$  and  $\theta$  are known, and so are the orientation parameters  $\sigma$  and  $\phi$  of the optic axis. Hence, we can find numerical solutions for  $\gamma''$  and  $\beta''$  that simultaneously satisfy all three Eqs (5), (6) and (7).

With the solutions for  $\gamma''$  and  $\beta''$  we can calculate the expected differential phase shift  $\Delta$  between the ordinary and the extraordinary ray (Born & Wolf, 1980):

$$\Delta = t_{\text{film}} (n''(\beta'') \cos(\gamma'') - n'(\beta') \cos(\gamma'))$$

This constitutes the exact solution for the expected retardance of the calcite film as a function of the aperture position. Examples of calculated retardance values are shown as solid lines in the graphs of Fig. 11.